EUROPEAN ORGANIZATION FOR NUCLEAR RESEARCH

CERN-PPE/91-129
19 August, 1991

Measurement of the Absolute Luminosity with the ALEPH Detector

The ALEPH Collaboration*

Abstract

We report on the absolute luminosity measurement performed with the ALEPH detector at LEP. The systematic errors of the measurements in 1990 are estimated to be 0.6% (experimental) and 0.3% (theoretical).

(Submitted to Zeitschrift für Physik C)

*See following pages for list of authors.

The ALEPH Collaboration

D. Decamp, B. Deschizeaux, C. Goy, J.-P. Lees, M.-N. Minard

Laboratoire de Physique des Particules (LAPP), IN^{2}P^3-CNRS, 74019 Annecy-le-Vieux Cedex, France

R. Alemany, J.M. Crespo, M. Delfino, E. Fernandez, V. Gaitan, Ll. Garrido, Ll.M. Mir, A. Pacheco

Laboratorio de Fisica de Altas Energias, Universidad Autonoma de Barcelona, 08193 Bellaterra (Barcelona), Spain[8]

M.G. Catanesi, D. Creanza, M. de Palma, A. Farilla, G. Iaselli, G. Maggi, M. Maggi, S. Natali, S. Nuzzo, M. Quattromini, A. Ranieri, G. Raso, F. Romano, F. Ruggieri, G. Selvaggi, L. Silvestris, P. Tempesta, G. Zito

INFN Sezione di Bari e Dipartimento di Fisica dell' Università, 70126 Bari, Italy

Y. Gao, H. Hu,[21] D. Huang, X. Huang, J. Lin, J. Lou, C. Qiao,[21] T. Ruan,[21] T. Wang, Y. Xie, D. Xu, R. Xu, J. Zhang, W. Zhao

Institute of High-Energy Physics, Academia Sinica, Beijing, The People's Republic of China[9]

W.B. Atwood,[2] L.A.T. Bauerdick, F. Bird,[4] E. Blucher, G. Bonvicini, F. Bossi, J. Boudreau, D. Brown, T.H. Burnett,[3] H. Drevermann, R.W. Forty, C. Grab,[23] R. Hagelberg, S. Haywood, J. Hilgart, B. Jost, M. Kasemann,[28] J. Knobloch, A. Lacourt, E. Lançon, I. Lehraus, T. Lohse, A. Lusiani, A. Marchioro, M. Martinez, P. Mato, S. Menary, A. Minten, A. Miotto, R. Miquel, H.-G. Moser, J. Nash, P. Palazzi, F. Ranjard, G. Redlinger, A. Roth, J. Rothberg,[3] H. Rotscheidt, M. Saich, D. Schlatter, M. Schmelling, M. Takashima, W. Tejessy, H. Wachsmuth, S. Wasserbaech, W. Wiedenmann, W. Witzeling, J. Wotschack

European Laboratory for Particle Physics (CERN), 1211 Geneva 23, Switzerland

Z. Ajaltouni, F. Badaud, M. Bardadin-Otwinowska, A.M. Bencheikh, R. El Fellous, A. Falvard, P. Gay, C. Guicheney, J. Harvey, P. Henrard, J. Jousset, B. Michel, J-C. Montret, D. Pallin, P. Perret, J. Proriol, F. Prulhière, G. Stimpfl

Laboratoire de Physique Corpusculaire, Université Blaise Pascal, IN^{2}P^3-CNRS, Clermont-Ferrand, 63177 Aubière, France

H. Bertelsen, F. Hansen, J.D. Hansen, J.R. Hansen, P.H. Hansen, A. Lindhal, R. Møllerud, B.S. Nilsson, G. Petersen

Niels Bohr Institute, 2100 Copenhagen, Denmark[10]

I. Efthymiopoulos, E. Simopoulou, A. Vayaki

Nuclear Research Center Demokritos (NRCD), Athens, Greece

J. Badier, A. Blondel, G. Bonneaud, J. Bourotte, F. Braems, J.C. Brient, G. Fouque, A. Gamess, R. Guirlet, S. Orteu, A. Rosowsky, A. Rougé, M. Rumpf, R. Tanaka, H. Videau

Laboratoire de Physique Nucléaire et des Hautes Energies, Ecole Polytechnique, IN^{2}P^3-CNRS, 91128 Palaiseau Cedex, France

D.J. Candlin, E. Veitch

Department of Physics, University of Edinburgh, Edinburgh EH9 3JZ, United Kingdom[11]

L. Moneta, G. Parrini

Dipartimento di Fisica, Università di Firenze, INFN Sezione di Firenze, 50125 Firenze, Italy

M. Corden, C. Georgiopoulos, M. Ikeda, J. Lannutti, D. Levinthal,[16] M. Mermikides, L. Sawyer

Supercomputer Computations Research Institute and Dept. of Physics, Florida State University, Tallahassee, FL 32306, USA [13,14,15]

A. Antonelli, R. Baldini, G. Bencivenni, G. Bologna[5], P. Campana, G. Capon, F. Cerutti, V. Chiarella, B. D'Ettorre-Piazzoli[6], G. Felici, P. Laurelli, G. Mannocchi[6], F. Murtas, G.P. Murtas, L. Passalacqua, M. Pepe-Altarelli, P. Picchi[5], P. Zografou

Laboratori Nazionali dell'INFN (LNF-INFN), 00044 Frascati, Italy

B. Altoon, O. Boyle, A.W. Halley, I. ten Have, J.L. Hearns, J.G. Lynch, W.T. Morton, C. Raine, J.M. Scarr, K. Smith, A.S. Thompson, R.M. Turnbull

Department of Physics and Astronomy, University of Glasgow, Glasgow G12 8QQ, United Kingdom[11]

B. Brandl, O. Braun, R. Geiges, C. Geweniger, P. Hanke, V. Hepp, E.E. Kluge, Y. Maumary, A. Putzer, B. Rensch, A. Stahl, K. Tittel, M. Wunsch

Institut für Hochenergiephysik, Universität Heidelberg, 6900 Heidelberg, Fed. Rep. of Germany[17]

A.T. Belk, R. Beuselinck, D.M. Binnie, W. Cameron, M. Cattaneo, P.J. Dornan[1], S. Dugeay, A.M. Greene, J.F. Hassard, N.M. Lieske, S.J. Patton, D.G. Payne, M.J. Phillips, J.K. Sedgbeer, G. Taylor, I.R. Tomalin, A.G. Wright

Department of Physics, Imperial College, London SW7 2BZ, United Kingdom[11]

P. Girtler, D. Kuhn, G. Rudolph

Institut für Experimentalphysik, Universität Innsbruck, 6020 Innsbruck, Austria[19]

C.K. Bowdery[1], T.J. Brodbeck, A.J. Finch, F. Foster, G. Hughes, N.R. Keemer, M. Nuttall, A. Patel, B.S. Rowlingson, T. Sloan, S.W. Snow, E.P. Whelan

Department of Physics, University of Lancaster, Lancaster LA1 4YB, United Kingdom[11]

T. Barczewski, K. Kleinknecht, J. Raab, B. Renk, S. Roehn, H.-G. Sander, H. Schmidt, F. Steeg, S.M. Walther, B. Wolf

Institut für Physik, Universität Mainz, 6500 Mainz, Fed. Rep. of Germany[17]

J-J. Aubert, C. Benchouk, V. Bernard, A. Bonissent, J. Carr, P. Coyle, J. Drinkard, F. Etienne, S. Papalexiou, P. Payre, B. Pietrzyk, Z. Qian, D. Rousseau, P. Schwemling, M. Talby[1]

Centre de Physique des Particules, Faculté des Sciences de Luminy, IN^{2}P^3-CNRS, 13288 Marseille, France

H. Becker, W. Blum, P. Cattaneo, G. Cowan, B. Dehning, H. Dietl, F. Dydak[26], M. Fernandez-Bosman, T. Hansl-Kozanecka,[2,22] A. Jahn, W. Kozanecki,[2] E. Lange, J. Lauber, G. Lütjens, G. Lutz, W. Männer, Y. Pan, R. Richter, J. Schröder, A.S. Schwarz, R. Settles, U. Stierlin, R. St. Denis, J. Thomas, G. Wolf

Max-Planck-Institut für Physik und Astrophysik, Werner-Heisenberg-Institut für Physik, 8000 München, Fed. Rep. of Germany[17]

V. Bertin, J. Boucrot, O. Callot, X. Chen, A. Cordier, M. Davier, G. Ganis, J.-F. Grivaz, Ph. Heusse, P. Janot, D.W. Kim[20], F. Le Diberder, J. Lefrançois[1], A.-M. Lutz, J.-J. Veillet, I. Videau, Z. Zhang, F. Zomer

Laboratoire de l'Accélérateur Linéaire, Université de Paris-Sud, IN^{2}P^3-CNRS, 91405 Orsay Cedex, France

D. Abbaneo, S.R. Amendolia, G. Bagliesi, G. Batignani, L. Bosisio, U. Bottigli, C. Bradaschia, M. Carpinelli, M.A. Ciocci, R. Dell'Orso, I. Ferrante, F. Fidecaro, L. Foà, E. Focardi, F. Forti, C. Gatto, A. Giassi, M.A. Giorgi, F. Ligabue, E.B. Mannelli, P.S. Marrocchesi, A. Messineo, F. Palla, G. Sanguinetti, J. Steinberger, R. Tenchini, G. Tonelli, G. Triggiani, C. Vannini, A. Venturi, P.G. Verdini, J. Walsh

Dipartimento di Fisica dell'Università, INFN Sezione di Pisa, e Scuola Normale Superiore, 56010 Pisa, Italy

J.M. Carter, M.G. Green[1], P.V. March, T. Medcalf, I.S. Quazi, J.A. Strong, R.M. Thomas, L.R. West, T. Wildish

Department of Physics, Royal Holloway & Bedford New College, University of London, Surrey TW20 OEX, United Kingdom[11]

D.R. Botterill, R.W. Clifft, T.R. Edgecock, M. Edwards, S.M. Fisher, T.J. Jones, P.R. Norton, D.P. Salmon, J.C. Thompson

Particle Physics Dept., Rutherford Appleton Laboratory, Chilton, Didcot, Oxon OX11 OQX, United Kingdom[11]

B. Bloch-Devaux, P. Colas, C. Klopfenstein, E. Locci, S. Loucatos, E. Monnier, P. Perez, J.A. Perlas, F. Perrier, J. Rander, J.-F. Renardy, A. Roussarie, J.-P. Schuller, J. Schwindling, B. Vallage

Département de Physique des Particules Elémentaires, CEN-Saclay, 91191 Gif-sur-Yvette Cedex, France[18]

J.G. Ashman, C.N. Booth, C. Buttar, R. Carney, S. Cartwright, F. Combley, M. Dinsdale, M. Dogru, F. Hatfield, J. Martin, D. Parker, P. Reeves, L.F. Thompson

Department of Physics, University of Sheffield, Sheffield S3 7RH, United Kingdom[11]

E. Bach, E. Barberio, S. Brandt, H. Burkhardt,[1] G. Gillessen, C. Grupen, G. Heitner, H. Meinhard, L. Mirabito, U. Schäfer, H. Seywerd, C. Stupperich, H. Trier, V. Zeuner

Fachbereich Physik, Universität Siegen, 5900 Siegen, Fed. Rep. of Germany[17]

G. Giannini, B. Gobbo, F. Ragusa,[25] L. Rolandi, U. Stiegler

Dipartimento di Fisica, Università di Trieste e INFN Sezione di Trieste, 34127 Trieste, Italy

L. Bellantoni, X. Chen, D. Cinabro, J.S. Conway, D.F. Cowen,[24] Z. Feng, D.P.S. Ferguson, Y.S. Gao, J. Grahl, J.L. Harton, J.E. Jacobsen, R.C. Jared,[7] R.P. Johnson, B.W. LeClaire, Y.B. Pan, J.R. Pater, Y. Saadi, V. Sharma, Z.H. Shi, Y.H. Tang, A.M. Walsh, J.A. Wear,[27] F.V. Weber, M.H. Whitney, Sau Lan Wu, G. Zobernig

Department of Physics, University of Wisconsin, Madison, WI 53706, USA[12]

[1] Now at CERN.
[2] Permanent adddress: SLAC, Stanford, CA 94309, USA.
[3] Permanent address: University of Washington, Seattle, WA 98195, USA.
[4] Now at SSCL, Dallas, TX, U.S.A.
[5] Also Istituto di Fisica Generale, Università di Torino, Torino, Italy.
[6] Also Istituto di Cosmo-Geofisica del C.N.R., Torino, Italy.
[7] Permanent address: LBL, Berkeley, CA 94720, USA.
[8] Supported by CAICYT, Spain.
[9] Supported by the National Science Foundation of China.
[10] Supported by the Danish Natural Science Research Council.
[11] Supported by the UK Science and Engineering Research Council.
[12] Supported by the US Department of Energy, contract DE-AC02-76ER00881.
[13] Supported by the US Department of Energy, contract DE-FG05-87ER40319.
[14] Supported by the NSF, contract PHY-8451274.
[15] Supported by the US Department of Energy, contract DE-FC0S-85ER250000.
[16] Supported by SLOAN fellowship, contract BR 2703.
[17] Supported by the Bundesministerium für Forschung und Technologie, Fed. Rep. of Germany.
[18] Supported by the Institut de Recherche Fondamentale du C.E.A.
[19] Supported by Fonds zur Förderung der wissenschaftlichen Forschung, Austria.
[20] Supported by the Korean Science and Engineering Foundation and Ministry of Education.
[21] Supported by the World Laboratory.
[22] On leave of absence from MIT, Cambridge, MA 02139, USA.
[23] Now at ETH, Zürich, Switzerland.
[24] Now at California Institute of Technology, Pasadena, CA 91125, USA.
[25] Now at Dipartimento di Fisica, Università di Milano, Milano, Italy.
[26] Also at CERN, PPE Division, 1211 Geneva 23, Switzerland.
[27] Now at University of California, Santa Cruz, CA 95064, USA.
[28] Now at DESY, Hamburg, Germany.

1 Introduction

Precise measurements of the Z boson parameters at LEP provide powerful tests of the Standard Model of electroweak interactions. The Z lineshape is measured by fitting a theoretical function [1], of the Z parameters to the cross sections for Z decay into fermion pairs at several centre of mass energies near the pole [2]. The dominant term in the cross section for production of a fermion pair $f\bar{f}$, at centre of mass energy $\sqrt{s}$, may be written[1]

$$\sigma_Z(s) = \frac{12\pi\Gamma_{e\bar{e}}\Gamma_{f\bar{f}}}{M_Z^2} \frac{s}{(s-M_Z^2)^2 + s^2\Gamma_Z^2/M_Z^2} \tag{1}$$

where M_Z is the Z mass, Γ_Z is the Z width, and $\Gamma_{e\bar{e}}$ and $\Gamma_{f\bar{f}}$ are the partial decay widths of the Z into electrons and fermions respectively. The measurement of the absolute luminosity plays a crucial role in determining the partial decay widths since they appear as overall factors effectively normalizing the cross sections. The systematic error on the absolute luminosity thus directly affects the error on each decay width.

A particularly important result from LEP has been the determination of the number of fermion families with light neutrinos, N_ν [2], [4]. Writing the peak cross section for Z decay into hadrons as

$$\sigma_{peak}^{(0)} = \frac{12\pi\Gamma_{e\bar{e}}\Gamma_{q\bar{q}}}{M_Z^2\Gamma_Z^2}, \tag{2}$$

then,

$$N_\nu = (\sqrt{\frac{12\pi R}{\sigma_{peak}^{(0)} M_Z^2}} - R - 3)/(\Gamma_{\nu\bar{\nu}}/\Gamma_{l\bar{l}}). \tag{3}$$

Here lepton universality is assumed (subscript l refers to any of the three charged leptons), R is the ratio of hadronic to leptonic decay widths, and $\Gamma_{\nu\bar{\nu}}$ is the Z partial decay width into one species of neutrino. The error on N_ν is now [2] dominated by the systematic error on the absolute luminosity, which appears in the error on $\sigma_{peak}^{(0)}$. Thus any deviations of N_ν from 3 which might signal new physics are dependent on a thorough understanding of the luminosity measurement. An error of 1% in the luminosity would change N_ν by 0.08 of a family.

The luminosity is determined by comparing the measured rate of low angle Bhabha scattering with the cross section predicted by the Standard Electroweak Model. Since the cross section falls rapidly with increasing scattering angle, it is important to define accurately the experimental acceptance in the region of the lowest scattering angles. In ALEPH the essential part of the acceptance is defined by comparing energy deposited on either side of a cell boundary in the luminosity calorimeter.

The total luminosity collected in 1990 for electroweak analysis [2] amounts to $6900.1 \pm 16.2(\text{stat}) \pm 48.3(\text{sys}) nb^{-1}$. In the following sections we describe the apparatus and the method used for the luminosity determination as well as the experimental and theoretical systematic errors.

2 The Apparatus

The ALEPH luminosity detector is an electromagnetic calorimeter (LCAL) with a track detector (SATR) in front (see figure 1). Technical details on the mechanical design

[1]The important effect of QED initial-state radiation is taken into account by integrating $\sigma_Z(s)$ over an initial state spectrum. [3]

and construction are described elsewhere [5]. The construction details which concern internal geometry and which are crucial to understanding the luminosity determination are repeated here. The luminosity measurement is based on energy deposits in LCAL. The SATR has been used for systematic checks.

2.1 The Luminosity Calorimeter

The calorimeter is a lead/proportional wire sampling device of nominal thickness 24.6 radiation lengths with 38 sampling layers. It is placed around the beam pipe on both sides of the interaction region with the first sampling layer at a distance of 266.8 cm from the nominal interaction point. The calorimeter covers a polar angle range, relative to the beam, from 45 mrad to 190 mrad. The calorimeter is mechanically subdivided into four semi-annular modules, each enclosed in its own gas–tight vessel. The outer radius is 52 cm and the inner radius is 10 cm. The depth of a module is 45 cm. On each side of the interaction region a pair of modules is joined together, resulting in an insensitive region in the vertical plane of 4 cm width. The LCAL modules are very similar to those of the ALEPH electromagnetic calorimeter [5].

The electromagnetic showers are sampled both on the anode and on the cathode of the shower detector sampling planes. The anodes are 20 μm thick gold–plated tungsten wires strung vertically inside extruded aluminium profiles with 5 mm spacing. The aluminium ribs separating wires are 0.5 mm thick. The wires are held by wire supports such that the free length never exceeds 38.6 cm. The cathodes are planes segmented into pads which are normally square, with a size which increases with distance from the interaction point. Typically, pads are 30 mm $\times$ 30 mm and usually six consecutive layers have pads of the same size. Along the edge of the sensitive area some pads have an irregular shape (see figure 2). The pads are internally connected to form towers pointing to the interaction point. Each tower is segmented into three longitudinal compartments called 'storeys'. The first, second and third storeys contain, respectively, 4.77 radiation lengths (9 sampling layers), 10.6 radiation lengths (20 sampling layers) and 9.25 radiation lengths (9 sampling layers with lead of double thickness). Analogue signals are available from each tower storey, from each of the 38 wire planes, and from the sum of the wire planes in each module. The shower energy and the longitudinal shower profile are measured using the anode wire signals. The wire signals contain no lateral information about the shower. The pad readout provides an energy measurement, a measurement of the lateral profile from which the shower centroid is reconstructed, and a rough longitudinal profile.

The modules are built on a 40 mm thick aluminium front plate which supports both LCAL and the SATR. The sampling layers are positioned by two 40 mm diameter bronze dowels passing through precision holes (80 μm larger than the dowels) in the layers and in the front and end plates. The extrusions and the printed circuit boards (PCBs) anchoring the wires are mounted on 0.5 mm aluminium sheets.

2.1.1 Survey of Cathode Pad Positions

Knowledge of the position of the acceptance regions is critical for the luminosity determination. Table 1 lists the relevant uncertainties. The uncertainties are listed in an order which starts with the printing of the PCBs (uncertainty # 1) and continues

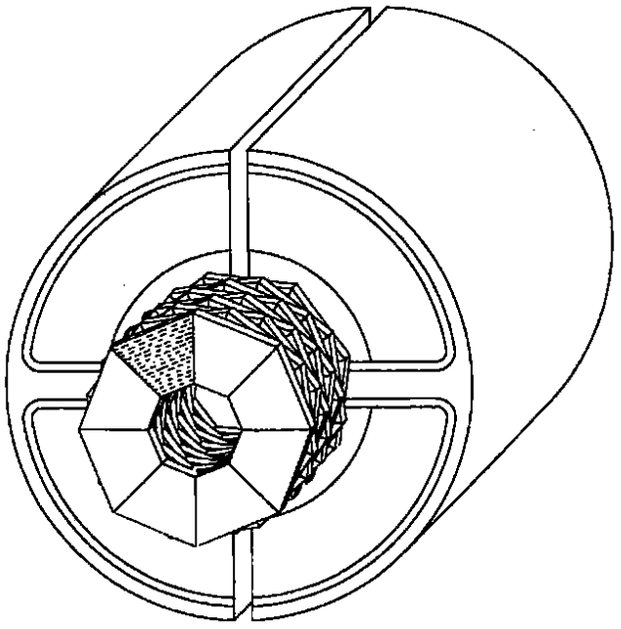

Figure 1: One endcap, showing the LCAL with the SATR mounted on its front plate. Each detector is made of two halves which fit around the beampipe.

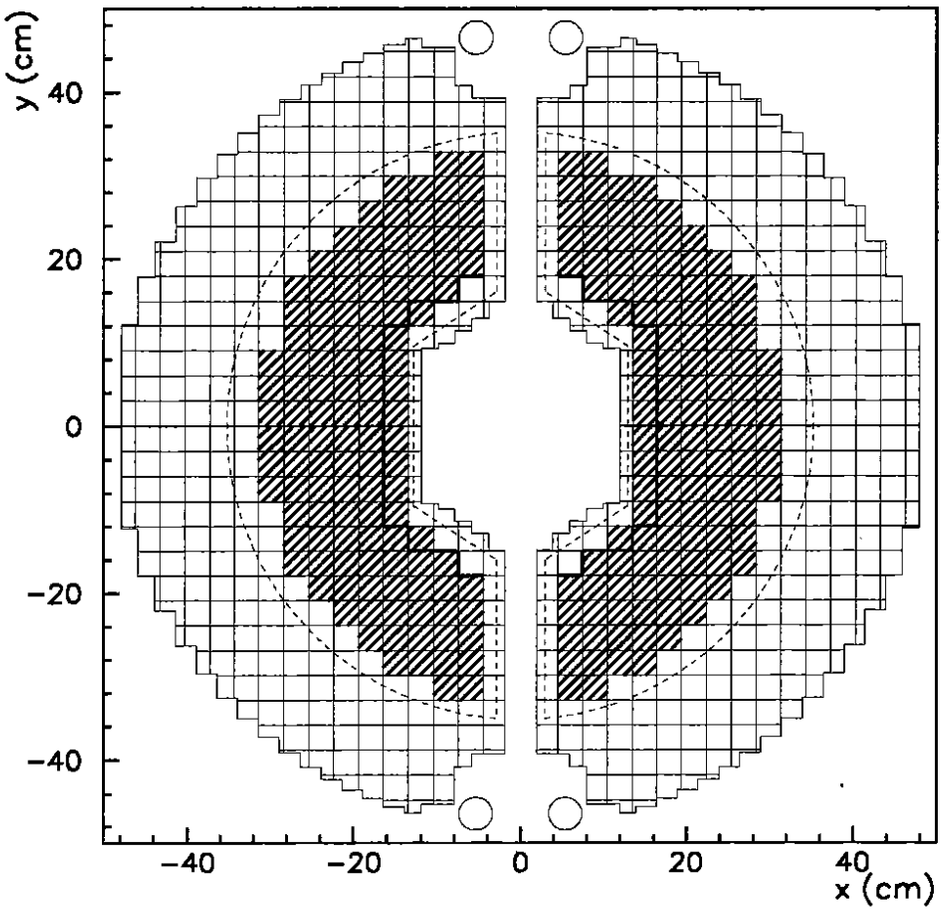

Figure 2: The active area of an LCAL module showing the fiducial (hatched) and non-fiducial (dashed outline) regions. The squares represent the PCB pads; they are shown at $z = 280$ cm, the average position of maximum energy deposition. The bold line shows the inner boundary of a more restrictive fiducial area which is used for systematic studies. The support dowels are also shown.

1) Relative position of pads	50 μm
2) Pads to PCB holes	50 μm
3) PCB holes to lead holes	50 μm
4) Lead holes to dowel holes	50 μm
5) Dowel holes to dowels	40 μm
6) Dowels to supporting holes	40 μm
7) Supporting holes to front reference marks	100 μm
8) Front reference marks to centre of supporting bar	60 μm
9) Effect of angular orientation	100 μm
Position uncertainty per module relative to centre of support bar	190 μm
Average uncertainty relative to centre of support bar	134 μm

Table 1: LCAL construction and survey uncertainties. Uncertainties 1-5 are common to all modules, while 6-9 are individual to each module.

through the stacking of the sampling layers (# s 2 - 5) and the mounting of the modules in ALEPH (# s 6 - 9).

The PCBs of a given size are made from a common print such that the uncertainty on the relative positions of the cathode pads inside a layer is 50 μm (# 1 in the table). We expect that this uncertainty is common for all boards of that size, and since most of the energy is deposited in a limited number of planes, 50 μm is taken to be the uncertainty on any distance between tower boundaries. The position of the PCB layers is fixed by means of steering pins through precision holes drilled in the PCB and the lead sheets, each with a tolerance of 50 μm (uncertainties 2, 3, and 4 in the table). The support holes in the lead sheets are positioned with respect to the dowels which carry the stack with a precision of 40 μm (# 5). These five uncertainties are common to all modules, while the remaining uncertainties are individual to each module.

The dowels are inserted into their support holes in the end plates with a position uncertainty of 40 μm (# 6). The positions of the support holes for the dowels in the front and end plate are known with respect to reference marks on the plates with an uncertainty of 100 μm (# 7). Two modules are connected at the face nearest the interaction point, at the top and bottom, using two horizontal support bars. The support bars connect to vertical legs which are in turn secured to the main structure of the ALEPH detector [5]. The dominant contribution to uncertainty (8) in the table is in the distance between the dowel holes in the support bars.

Since the modules are not connected together at the back, there can exist a small non-zero opening angle between the modules. The uncertainty in this angle is equivalent to an uncertainty in the horizontal position of the modules. The opening angle is determined by survey, and checked by comparing positions of SATR tracks with LCAL clusters as discussed in section 7.

The positions of the modules in space are based on a precision optical survey. The survey was repeated at four different times during 1990. Each survey measured three or four points on each module, depending on line-of-sight access at the time. Comparison of the surveys shows that the centre position of each pair is determined with a precision of 0.32 mm in the radial direction and 0.85 mm in z.

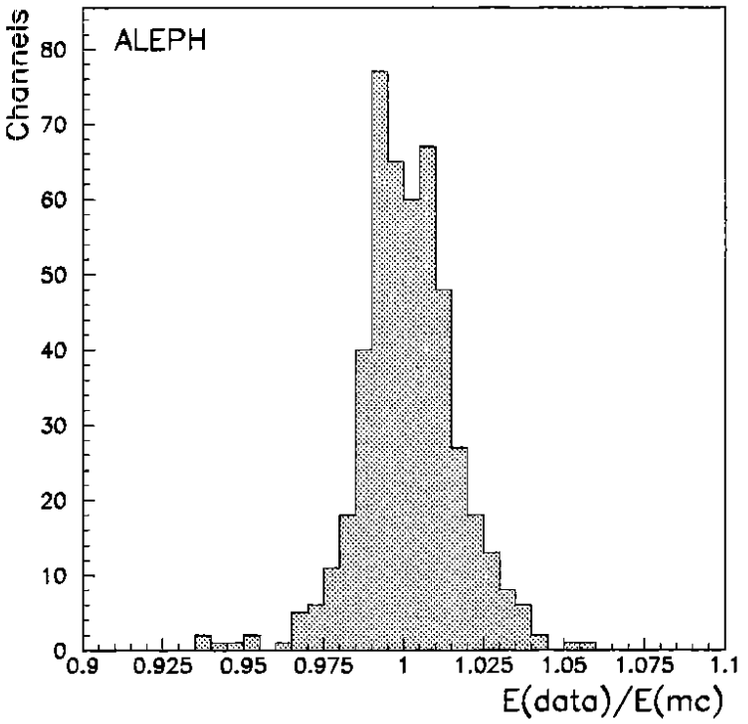

Figure 3: Distribution of ADC channel gains normalized to the gain expected from Monte Carlo for cells in the fiducial region.

The opening angle uncertainty (# 9) is estimated from the internal consistency of the different surveys.

Combining the uncertainties from table 1 in quadrature results in an uncertainty of 0.190 mm in the radial position of a tower. Reducing, by a factor of $\sqrt{4}$, the uncertainties that are individual to each module results in an average uncertainty of 0.134 mm. This average uncertainty is relevant because the main event selection cut is a requirement on the shower position in one module (see section 4). Thus the luminosity is to some extent the average of that in the four LCAL modules.

2.1.2 Energy Measurement

The pedestal for each channel was maintained and updated online through regular measurement. These pedestals were used for zero-suppression. The pedestals for channels using a common electronic circuit were continually updated during reconstruction using data from a non-zero-suppressed channel which shared the same circuit.

After event reconstruction a calibration factor which depends on LEP fill and LCAL module number was determined from e^+e^- events which were very collinear and which avoided insensitive zones in the detector. The precision of the calibration is limited by run statistics to about 0.5% .

No channel dependent calibration of the gains was applied. The systematic error on the luminosity from variations in cell-to-cell gain are discussed in section 7.5. Figure 3 shows the observed average energy for each channel divided by the Monte Carlo expectation for that channel, for which the gain is assumed to be constant. The figure

shows that the channel-to-channel variations are 1.4% (r.m.s) over the acceptance region.

2.2 The Small Angle Tracker

The Small Angle Track detector (SATR) consists of nine layers of drift tube chambers. The tubes are arranged in a staggered octagonal configuration, and are mounted on the front plate of the LCAL. The SATR covers a polar angular region from 41 mrad to 90 mrad. Each layer is made of eight 45° sectors, each of which contains 14 drift-tubes. Each successive layer is rotated by 15° with respect to the previous layer to avoid having dead zones. This results in three sets of planes with different orientations.

The individual drift cells forming one 45° sector are made from brass tubes with a square cross section of 9.95×9.95 mm^2 outer dimension and a wall thickness of 300 μm. The positioning of the 25 μm anode wires is guaranteed by notches cut in precision epoxy supports such that the uncertainty in their position with respect to the brass dowels carrying the SATR structure is below 60 μm. Individual drift tubes were chosen as detector elements to fight the anticipated high background due to synchrotron radiation at LEP which would have caused serious problems for track reconstruction if low density material drift chambers without separating walls had been used instead.

The amount of material in front of the SATR varies between 14% and 7.3% of a radiation length in the angular range from 40 to 90 mrad. The amount of material in the tracker itself represents 67% of a radiation length.

2.2.1 Performance

The spatial resolution for Bhabha-scattered electrons is dominated by the presence of secondary electrons which are detected in the single-hit electronics of SATR. This resolution leads to an r.m.s. error on the track polar angle of 0.31 mrad [6]. The azimuthal resolution of the entire chamber was found to be about 25 mrad. These values correspond to an r.m.s. error of the fitted track position of 800 μm in the radial direction and 3.8 mm in azimuth. The SATR was surveyed together with the LCAL.

3 Triggers

The triggers used in the luminosity determination are designed to be redundant and highly efficient, and to allow measurement of trigger efficiency and backgrounds. There are two main triggers for Bhabha events: the first uses the tower energies and requires a coincidence between the electron and the positron sides with more than 22 GeV on one side and 10 GeV on the other side. The other main trigger uses energies from the wire planes and requires a coincidence of each side having more than 10 GeV, and the sum above 45 GeV. The efficiency of each of these triggers is monitored using two other triggers which require energy in only one module of the detector. The thresholds for these additional triggers are 35 GeV for both the towers and wire planes. There are other triggers with lower thresholds which are prescaled and which are used to measure the thresholds of the main triggers and to study background from off-momentum beam particles.

Additionally, for part of the 1990 data taking, there was a prescaled trigger from the SATR which requires eight SATR planes to fire in modules opposite in z and ϕ. This trigger is vetoed by the presence of hits in the inner tracking chamber [5].

4 Selection of Events

Bhabha events are selected on the basis of energy clusters in the calorimeter. Clusters are made by joining together towers for which two storeys, containing more than 50 MeV, share a common side or corner. Towers from different modules are not joined. The analysis uses the central nine towers in any cluster, i.e. the highest energy tower and its eight nearest neighbours. Only the highest energy cluster in each endcap is considered.

The selection of Bhabha events is very simple: one cluster is required to be inside a restricted (fiducial) region of the calorimeter, the other cluster must be inside a less restricted (non-fiducial) region. Requirements are made on the energy of each cluster and on the sum of the energies. Finally, the clusters are required to be coplanar. In the following paragraphs the event selection is described in more detail.

The fiducial and non-fiducial regions are shown in figure 2. One endcap is defined as the fiducial side on each ALEPH trigger, the other being the non-fiducial side. The choice of fiducial side alternates on each trigger. The alternation ensures that the acceptance is independent, to first order, of transverse and longitudinal displacements of the collision point, and of small angular changes of the beam direction (see section 7.3).

The fiducial region excludes towers along the inner edges of the calorimeters, and also a region at large angles which is in the shadow of material from the central detectors. To pass the fiducial side geometric selection the most energetic triplet of towers parallel to the boundary must be contained in the fiducial region. When the tower with the highest energy is at a corner of the fiducial region then the requirement is made in both directions. Only the energy in the first two storeys is used in this geometrical selection. We will define a second, more restrictive fiducial region for use in studying systematic errors. The tighter boundary, shown in figure 2, excludes an additional pad along the inner edge of the detector.

On the non-fiducial side the acceptance region is defined using the cluster centroids. The centroid of a cluster is calculated by weighting the centre of each tower with the corresponding energy fraction. The non-fiducial region is defined, near the inner edge of the calorimeter, to be 10 mm inside the edge of the sensitive area. The edge of the non-fiducial region at high angle extends to 125 mrad (see figure 2).

The distribution of normalized fiducial cluster energies E_1/E_{beam} versus that for non-fiducial cluster E_2/E_{beam}, is shown in figure 4(a); the line on the plot indicates the energy cuts used in the analysis. The normalized sum of fiducial and non-fiducial cluster energies are shown in figure 4(b) and the individual cluster energies, normalized to the beam energy, are shown in figures 4(c) and (d). In each plot all cuts have been applied except those for the quantity (or quantities) plotted. The beam-related background is concentrated at low E_1 and E_2. It is mostly removed by the energy cuts and a cut on difference in azimuthal angle. The energy cuts require that both E_1 and E_2 exceed 44% of the beam energy, and that their sum exceeds 60% of the centre of mass energy. The energy distribution is generally well simulated. The excess of data at high energy comes from overlapping off-momentum beam particles.

In order to reduce background further, the difference in the azimuthal angle between the two cluster centroids is required to satisfy $170^0 < \Delta\phi < 190^0$. The distribution of this quantity for real and simulated data is shown in figure 5. The peak is displaced

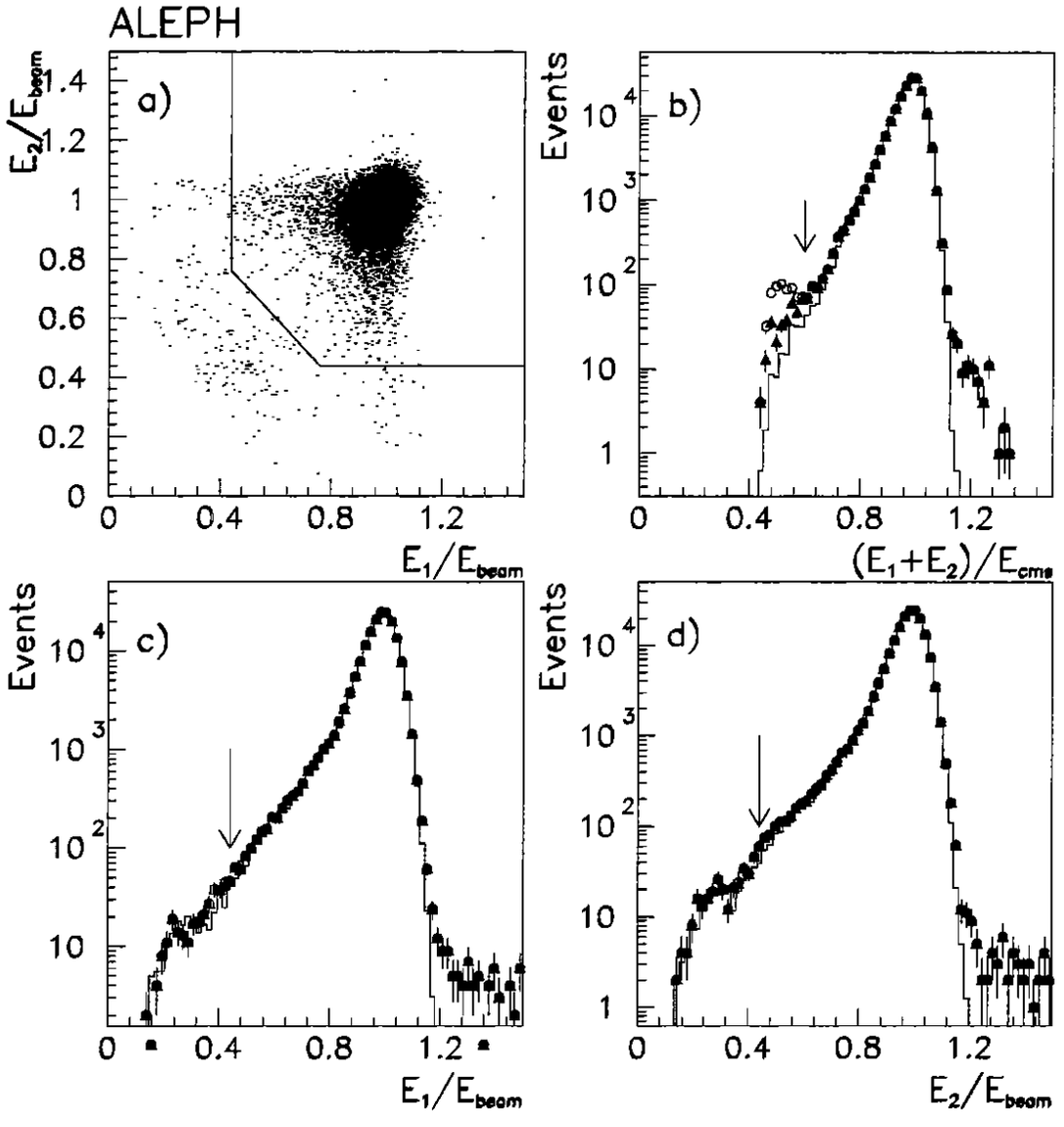

Figure 4: Energy distributions in LCAL normalized to the beam energy. For clarity only about 10% of the data are shown in plot (a), all other plots show all the data and the Monte Carlo normalized to the data. The Monte Carlo is shown as a solid histogram, the data as solid points. Data without background subtracted is shown as open points. The line in (a) shows the cuts which are indicated by arrows in (b-d). In each plot all cuts, including fiducial and non-fiducial requirements and the $\Delta\phi$ cut, are applied except those for the energy (energies) plotted. (a) Energy on the fiducial side, E_1, versus that from the non-fiducial side, E_2, data only. (b) The sum of E_1+E_2 for data and Monte Carlo. (c) E_1 for data and Monte Carlo. (d) E_2 for data and Monte Carlo.

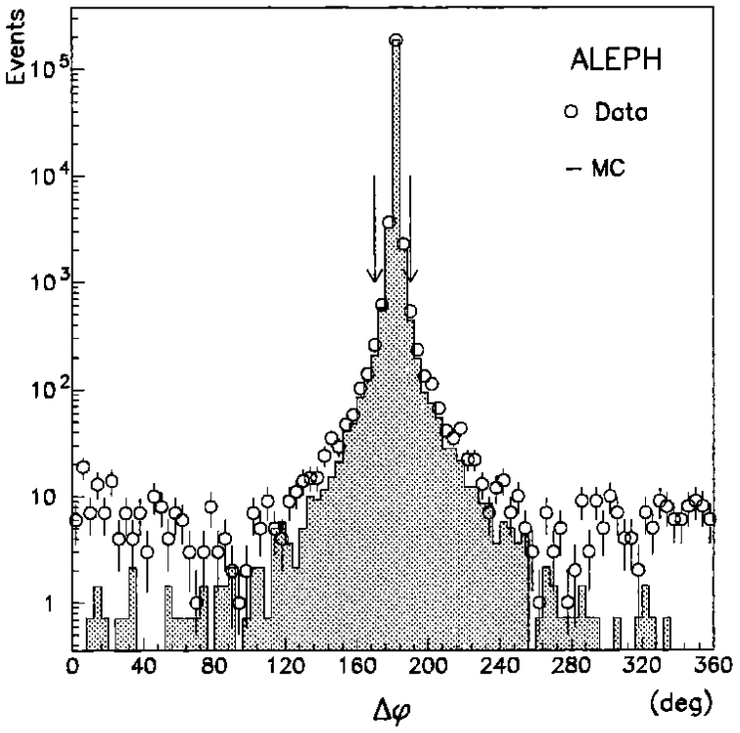

Figure 5: The difference in azimuth, $\Delta\phi$, between the two clusters. Bhabha events are evident as the large peak. Background from random coincidence of off–momentum particles populates the sides of the distribution.

from 180^0 by the magnetic field (1.5 T in the e^--direction). The excess of data on the wings of the distribution is caused by random coincidences of off-momentum beam particles.

5 Background

The selection criteria eliminate most of the background from off-momentum beam particles. The number of remaining background events from this source is estimated by counting the events which pass all the selection criteria except the cut on $\Delta\phi$ but which have a $\Delta\phi$ value in one of the side intervals 0° to 10° and 350° to 360° (see figure 5). This is a good estimator of the beam related background, since fake background events constructed from single arm triggers occur with similar frequency in the side intervals as in the signal region. The ratio of the number of fake reconstructed events in the side intervals to that in the signal region is 0.92 ± 0.12. In this way a contamination of (0.014 ± 0.004)% is found.

Genuine non-Bhabha interactions cause very little background. A sample of events corresponding to 20 pb^{-1} of two–photon collisions has been simulated. After applying the selection criteria on the simulated events, a contamination of $1.4 \cdot 10^{-5}$ [7,8] of the accepted Bhabha sample is found.

The reaction $e^+ + e^- \rightarrow \tau^+ + \tau^-$, where each tau decays into an electron or a neutral meson, could contribute. A contamination of $0.4 \cdot 10^{-5}$ is derived from a Monte Carlo sample corresponding to 20 pb^{-1} [8].

The contribution from $q\bar{q}$ events is assumed to be less than the $\tau\bar{\tau}$ contribution.

A check on the combined two–photon background and the $q\bar{q}$ background is made by counting accepted events with a track seen in the central detector. Such events constitute 0.02% of the Bhabha events. This must be regarded as an upper limit on the background, since converted radiative photons from Bhabha events contribute.

The background from t-channel production of two hard photons is estimated by Monte Carlo simulation to be $(0.069 \pm 0.003)\%$ [6,7,8]. The signature for this process in the data would be perfectly collinear energy deposits in the LCAL with no tracks found in the SATR. To estimate the rate of such events in the data, a fit to the $\Delta\phi$ distribution of events with no SATR tracks has been made using two Gaussians of the same width with one of them centred at 180°. In this way a photon contamination of $(0.05 \pm 0.01)\%$ relative to the total sample has been measured (we subtract the measured 0.05% from our cross section).

In total a background contamination of $(0.09 \pm 0.03)\%$ is subtracted from the signal.

6 The Bhabha Cross Section

As stated in the introduction, the luminosity is determined by comparing the measured rate of Bhabha scattering with the cross section predicted by theory. For the prediction we use the event generator BABAMC [9] for the reaction $e^+e^- \rightarrow e^+e^-(\gamma)$. The generated events are passed through a detector simulation which produces simulated "raw data". The "data" are then reconstructed and analyzed using the same programs as the for real data. In order to save computer time a preselection is made on the events before passing them to the full detector simulation: among the generated events, only those which contain particles in the active volume of the detector carrying at least 10% of the collision energy on each side, or at least 35% of the energy in total, are passed through the detector simulation. A reference cross section, σ_{ref}, at a particular beam energy, is calculated from the Monte Carlo events using the same cuts as are used on the data. The luminosity at that energy is then given by:

$$L = \frac{N_{Bhabha}}{\sigma_{ref}}$$

where N_{Bhabha} is the number of events in the data passing the selection cuts.

Monte Carlo events were generated at a collision energy $\sqrt{s}_{ref}$ of 91.0 GeV and at scattering angles between 15 mrad and $\pi/2$, with the additional input of a Z mass, M_{ref}, of 91.17 GeV, a 150 GeV top quark, a 250 GeV Higgs boson, and an infrared cut-off parameter[2] k_0 of 0.001. A correction of $1.5 \cdot 10^{-4}$ has been applied to account for events with electron and positron scattered into the backward hemispheres, which have not been passed through the full detector simulation. The program internally calculates a Z width, $\Gamma_{ref} = 2.475$ GeV. The reference cross section, σ_{ref}, for our acceptance is found to be $(26.30 \pm 0.16_{exp} \pm 0.08_{theory})$ nb; the errors are discussed in the following sections.

The cross section σ at other collision energies is found using the phenomenological parametrization shown in figure 6. The points show the BABAMC cross section at energies near the Z peak, normalized to σ_{ref} and with the $1/s$ dependence divided out. The curve reproduces the BABAMC points to within one part per mil. The effect on fitted parameters due to this correction is small, except for the Z mass, where the

[2]The infrared cut-off k_0 separates the elastic scattering contribution from hard bremsstrahlung. This cut–off is a technical necessity in Monte Carlo programs and no result should depend on its value.

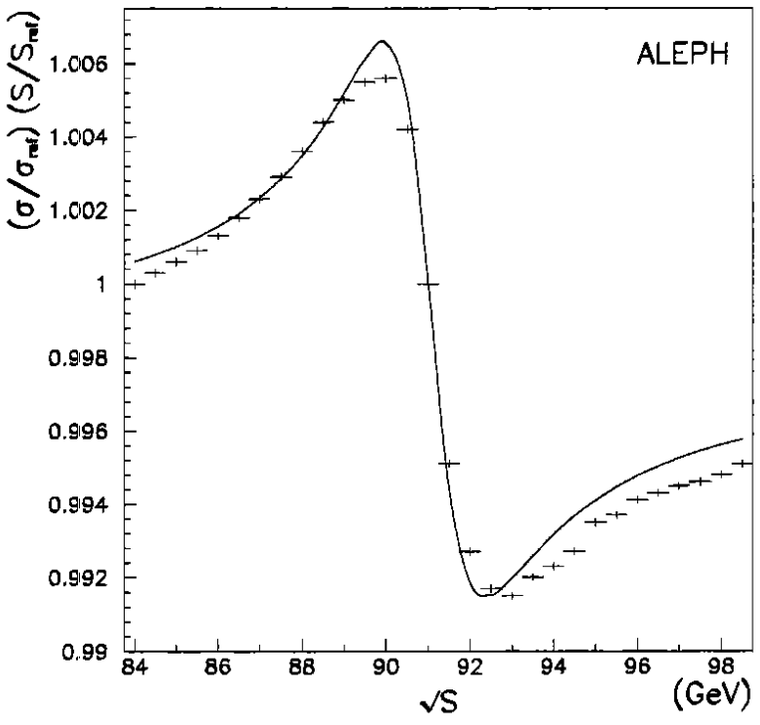

Figure 6: The electroweak correction applied to the Bhabha cross section as a function of centre of mass energy (solid curve). The vertical axis shows the Bhabha cross section normalized to the reference cross section. The photon-exchange dependence on $1/s$ is also divided out. The points are from BABAMC.

correction is of the same size as the ALEPH statistical error (which is smaller than the uncertainty of ± 20 MeV on the overall LEP energy scale). If the correction is ignored the resulting Z mass will be artificially 10 MeV high, and the Z width will be 2 MeV high. Ignoring the correction results in a hadronic peak cross section which is 0.13 nb high, which means that the number of neutrinos will be underestimated by 0.03. The uncertainties in the fitted parameters due to the inadequacy of the parametrized curve are about 10% of the total correction to each parameter, e.g. about 1 MeV for the Z mass.

7 Errors in the Luminosity Determination

The experimental systematic errors on the Bhabha cross section result from uncertainties in the simulation, calibration, and positioning of the calorimeter, as well as Monte Carlo statistics. The verification of the errors is limited by the statistics of the data (180,000 accepted events in 1990) and the Monte Carlo simulation (283,000 accepted events).

A summary of systematic errors is given in table 2. The individual contributions are described in the following sections.

Background estimate (sect. 5)	0.03%
Trigger efficiency (sect. 7.1)	nil
Alignment and mechanical tolerances of one module (sect. 7.2)	0.24%
Beam parameters and position of the centre of two modules (sect. 7.3)	0.02%
Position resolution, vertex spread and beam divergence (sect. 7.4)	nil
Fiducial side cut (sect. 7.5)	0.38%
Non–fiducial side cut (sect. 7.6)	0.15%
$\Delta\phi$ cut (sect. 7.7)	0.10%
Energy cut (sect. 7.8)	0.23%
Approximation of energy dependence (sect. 6)	0.10%
Statistics of simulation (sect. 7, introduction)	0.19%
Total experimental uncertainty	0.6%

Table 2: Summary of experimental systematic errors in the luminosity measurement.

7.1 Trigger Efficiency

The inefficiency of the main trigger based on signals from the wires has been measured using the tower-based triggers and the single-arm triggers while assuming that the two sides of the detector are independent. The wire trigger inefficiency is found to be 0.001%. The tower-based triggers are also nearly fully efficient, the inefficiency being 0.006% for all but a single period comprising 3% of the data. During that time there was a problem in the pad trigger electronics and a section of the pad trigger had to be turned off, reducing the pad trigger efficiency to 75%. Including this period the pad trigger inefficiency is 0.8%. The overall trigger inefficiency is negligible, assuming no correlation between the wire and pad triggers.

The SATR triggers have been used to estimate the inefficiency that might arise from a correlated failure of all the LCAL triggers, such as a high voltage trip, which the monitoring system fails to detect. No inefficiency in the LCAL is found for the running period of the SATR triggers, which comprised about 1/3 of the data. In conclusion, the trigger efficiency is taken to be 100% and no systematic error is assigned from this source.

7.2 Relative Position of the Fiducial Region

The position of the fiducial regions relative to the centre of a pair of modules determines the inner edge of the acceptance region and thus strongly influences the Bhabha counting rate. SATR is used to check whether this position is correctly simulated. Events with polar angle larger than 60 mrad are used and the trajectories are extrapolated to $z_{ref} = 280$ cm, the plane of the average shower maximum. There the average radial displacement of LCAL with respect to SATR is found to be -0.11 mm in the data and -0.17 mm in the Monte Carlo. The agreement is well within the expected position error of 0.16 mm obtained by combining LCAL and SATR tolerances. The average interaction point position as determined by the ALEPH tracking detectors was used in the Monte Carlo generation.

More importantly, in order to check directly the placement of the fiducial boundary, the accepted fraction of the events is shown in figure 7 (a) as a function of the horizontal

coordinate, x, measured by SATR for events near the horizontal plane. From a fit to the distribution, a difference is found in the halfheight position between data and Monte Carlo of (-0.05 ± 0.10) mm (where the error comes from changing fit ranges). figure 7 (b) shows the same distribution for events selected with another choice of fiducial boundary which is moved one tower away from the beam along the inner edge (see figure 2). Here, the difference is (-0.14 ± 0.10) mm. Both differences are consistent with the difference in radial displacement observed above.

Since the comparisons are affected by uncertainties in positioning and simulation of both LCAL and SATR, as well as statistics, we take as the relative position uncertainty the nominal average uncertainty of the LCAL inner radius of 0.134 mm from table 1.

Considering only the dominant term in Bhabha scattering, an uncertainty Δr_{min} on the effective inner radius results in a luminosity uncertainty given approximately by:

$$\frac{\Delta L}{L} = 2 \cdot \frac{\Delta r_{min}}{r_{min}} \cdot \frac{1}{1 - (r_{min}/r_{max})^2}. \tag{4}$$

For our acceptance $r_{min} = 150$ mm is the average minimum radius and $r_{max} = 300$mm is the average maximum radius. This leads to an uncertainty of 0.24%, which is confirmed by a numerical integration of the dominant term of the cross section over our complicated fiducial and non-fiducial acceptance with the approximation of allowing only collinear radiation.

7.3 Beam Parameters and the Position of the Centre of Two Modules

Moving or tilting the beam is equivalent to a displacement or tilt of the detector. An estimate for the error in the luminosity introduced by such an effect is:

$$\frac{\Delta L}{L} = 2 \cdot (\frac{\Delta r}{r_{min}})^2 \tag{5}$$

where Δr is the effective shift of the centre of two modules. This expression is valid as long as Δr is small compared to the distance between the fiducial and non–fiducial boundaries. The effects on the luminosity of beam displacements are shown in more detail in figure 8. Also shown in figure 8 is the transverse beam position as reconstructed from the shower positions and assuming the particles to be emitted collinearly. The effect of an unknown beam displacement would be seen as a difference in the means of the Monte Carlo and data distributions in the figure. The means calculated from data and Monte Carlo in figure 8 agree within 0.2 mm. An uncertainty of 0.2 mm in the transverse beam position corresponds to a negligible (less than 0.001%) uncertainty in the ALEPH luminosity.

Longitudinal uncertainty in beam position has a negligible (less than 0.002%) effect on the ALEPH luminosity, for reasonable variations in the collision point position. As mentioned previously, this insensitivity is due to the fact that the roles of fiducial and non–fiducial endcaps are exchanged on each trigger.

An unknown beam tilt in the horizontal plane would manifest itself as a difference in counting rate in the two pairs of opposing LCAL modules. Such a counting rate difference could also arise on account of the positions of the detector modules. The positions of the detectors, as determined from the survey, are incorporated in the Monte Carlo. The fractions of the luminosity seen by the two pairs of opposing modules are (50.9 $\pm$0.2)% and (49.1 $\pm$0.2)% in the data. In the Monte Carlo the fractions are (51.0

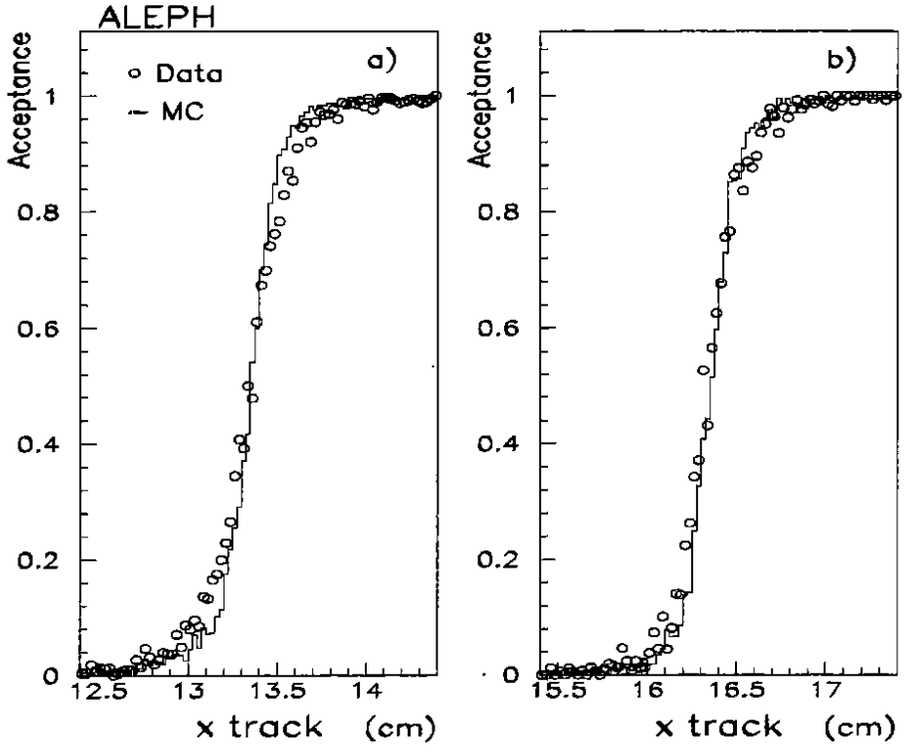

Figure 7: The acceptance at the inner boundary near the horizontal plane as measured by SATR. The x position is measured by SATR. Each bin contains the fraction of events accepted by the LCAL at that value of x. (a) shows the accepted fraction for the standard fiducial boundary, in (b) the fiducial boundary has been moved one pad row away from the beamline.

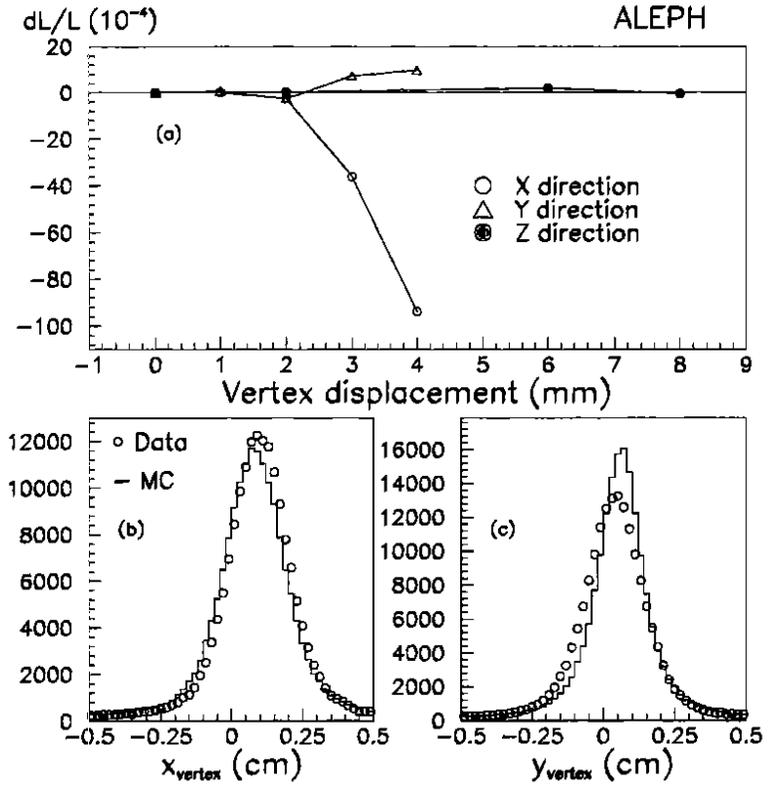

Figure 8: (a) Change in luminosity for different beam displacements. (b) The horizontal transverse vertex position as measured by LCAL (at z=0.0) for data and Monte Carlo. (c) The vertical transverse vertex position. The transverse vertex positions in data and Monte Carlo agree to within 0.2 mm.

± 0.2)% and (49.0 ± 0.2)%. Thus no unaccounted for large tilt in the horizontal plane is evident. There is no direct fill–to–fill measurement of the absolute direction of the beam with respect to ALEPH. Within a LEP fill the changes in the horizontal beam direction are controlled to about ± 0.25 mrad. A tilt of this magnitude would change the luminosity by about 0.01%.

In the vertical direction the relative changes in the beam direction during a fill are controlled to about ± 1 mrad. A change of this size in the vertical beam direction would change the ALEPH luminosity by about 0.02%. Adding this uncertainty quadratically to that due to horizontal beam tilt gives a total uncertainty from beam parameters and endcap positions of 0.022%.

7.4 Position Resolution

The polar angle resolutions for LCAL and SATR have been estimated by comparing cluster positions as measured by LCAL with track positions from SATR (see section 7.2). Unfolding the resolutions for the individual detectors reveals a polar angle resolution for LCAL of (0.51 $\pm$ 0.01) mrad, which implies an error σ_{LCAL} of (1.43 $\pm$ 0.01) mm in the radial position (at the longitudinal position of shower maximum). The SATR polar angle resolution is found to be 0.31 mrad.

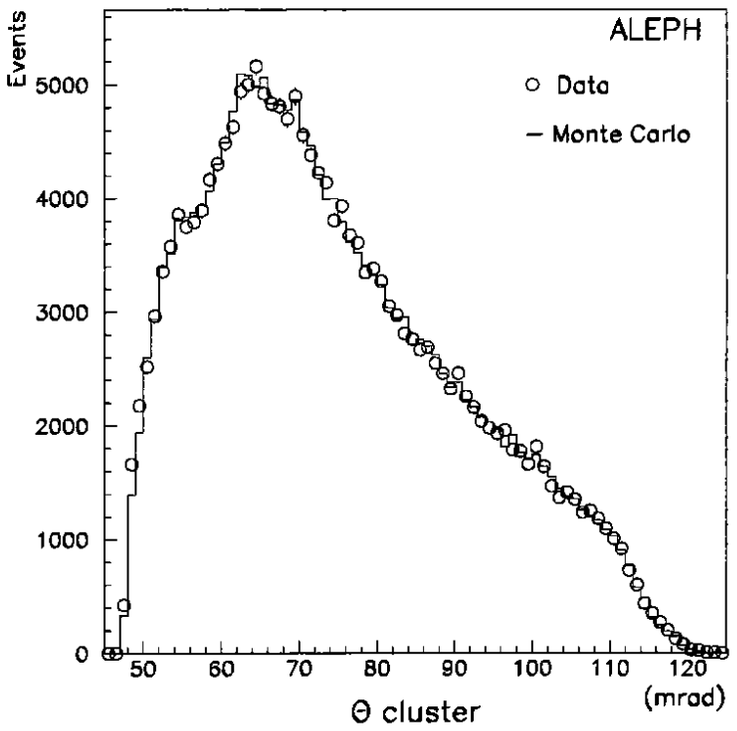

Figure 9: Distribution of the polar angle of accepted LCAL clusters on the fiducial side.

An error $\Delta\sigma_{LCAL}$ in the simulated resolution would change the luminosity by roughly

$$\frac{\Delta L}{L} = 3 \cdot \frac{\Delta\sigma^2_{LCAL}}{r^2_{min}}. \tag{6}$$

An error in the beam position spread or divergence contributes in the same manner. The LEP beam divergence at ALEPH is roughly 0.25±0.05mrad, but was set to zero in the Monte Carlo generation. The full 0.25 mrad ($\approx$ 0.7 mm at the longitudinal position of shower maximum) is taken as the error in the beam divergence, which then dominates the uncertainty in the detector resolution. Using $\Delta\sigma^2_{LCAL} = (0.7 \text{ mm})^2$ and $r_{min} = 150$ mm, the error in the luminosity from this source is negligible.

7.5 Fiducial–Side Cut

Errors in material simulation or cell-to-cell calibration could produce a shift in the effective fiducial boundary position. The good overall agreement between data and Monte Carlo on the geometrical acceptance is illustrated in figure 9, showing the distribution of cluster polar angles, and in figure 10, showing the distribution of azimuthal angles. As mentioned earlier, we observe reasonable agreement between the acceptance in the data and Monte Carlo seen by the SATR tracks when moving the fiducial boundary (see section 7.2). However the difference in luminosity actually measured using the tighter boundary and the standard boundary is $(-0.38 \pm 0.19)\%$, where the error is purely statistical. Variations in the exact position of the boundary of the non-fiducial area, when made in conjunction with the change in fiducial area, have little effect on the

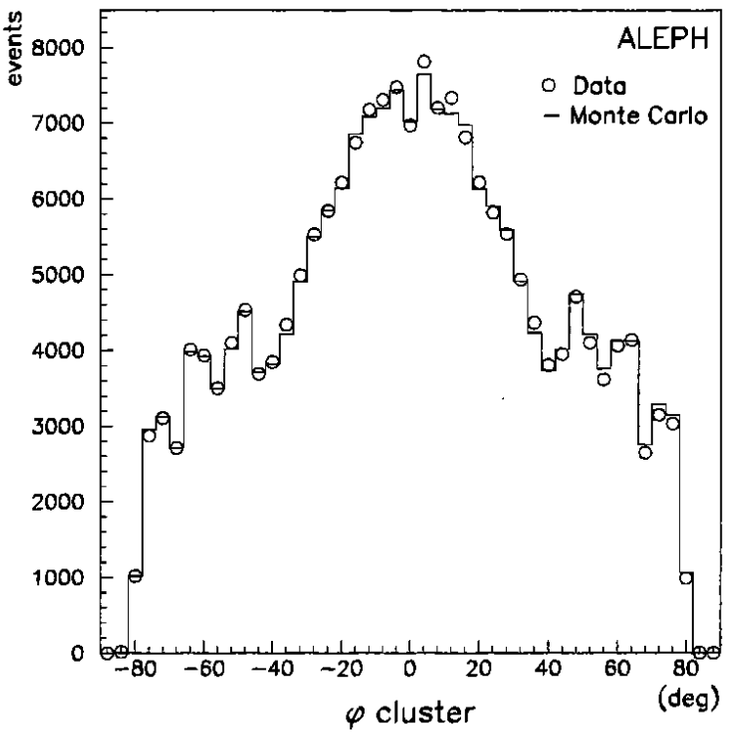

Figure 10: Distribution of the azimuthal angle of accepted LCAL clusters on the fiducial side.

observed difference of -0.38%. The difference expected from higher order corrections when the fiducial boundary is moved is $(-0.08\pm\ 0.03)\%$ (see section 9).

The mechanical uncertainties discussed in section 7.2 cannot explain the difference since, with the exception of item 1 of table 1, they affect both the standard and tighter boundary measurements similarly. The uncertainty in luminosity implied by item 1 of table 1 is only $\pm 0.09\%$, using equation 4.

In the search for an explanation for such discrepancies the simulation of the shower shape has been investigated. Figure 11 compares data and simulation for the transverse cluster size and the energy fractions in the three storeys. The transverse size is taken as the r.m.s. spread of tower centres belonging to the cluster. It is found to be 23.43 ± 0.03mm in the data, and 23.48 ± 0.03 mm in the Monte Carlo. The width in the Monte Carlo would have to be 2.7 mm larger to explain the difference in luminosity observed. In fact the width is expected to be slightly *larger* in the data than in Monte Carlo due to overlapping background clusters which are not in the Monte Carlo.

Because the towers are not perfectly projective, the simulation of the longitudinal shower development also matters. The standard selection is based on the energy in the first two storeys, where the second dominates. An event selection on the fiducial side using only the first storey gives a relative change in the number of events of $(-0.17 \pm 0.02)\%$ in the data and $(-0.30 \pm 0.04)\%$ in the Monte Carlo. The change in luminosity is $(0.13 \pm 0.05)\%$ [8].

Finally, a relative energy calibration error on the two sides of the fiducial boundary could change its effective radius. The observed cell-to-cell variations along the boundary

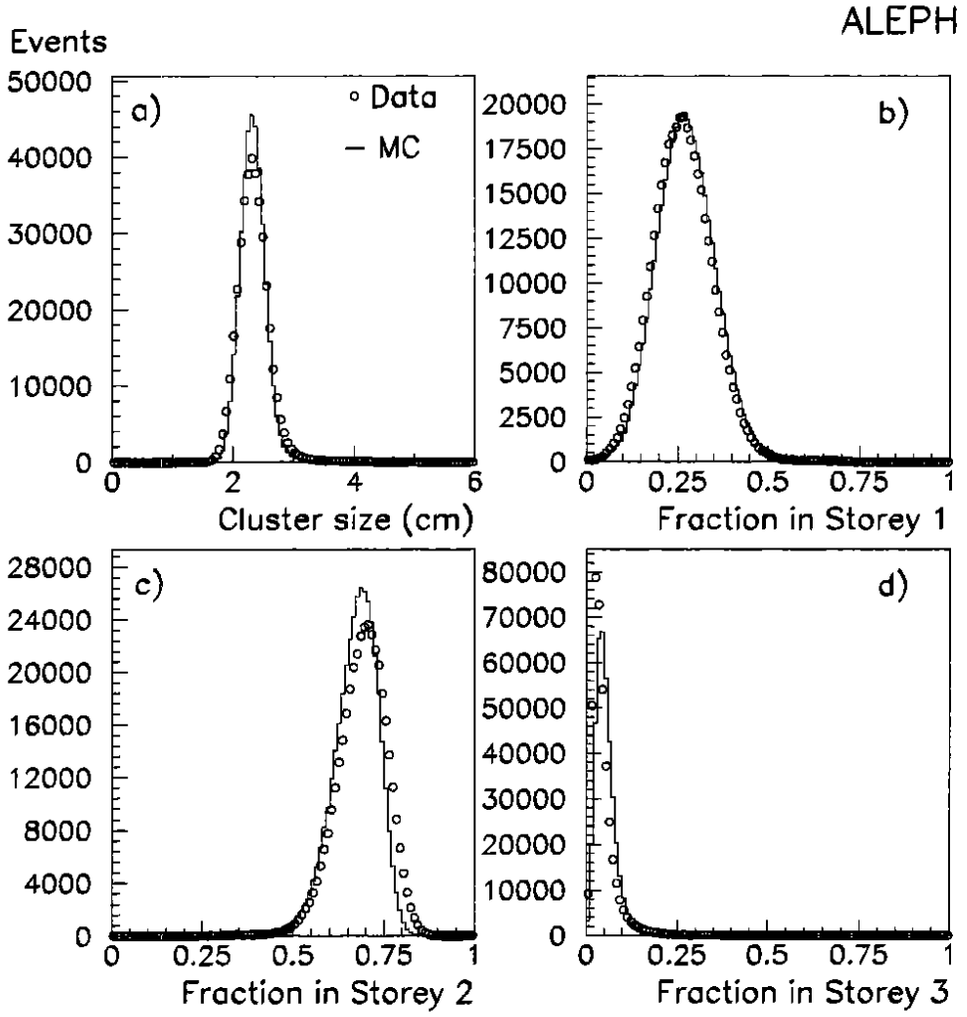

Figure 11: Comparison of shower shape variables. (a) the transverse size, (b) the energy fraction in storey 1, (c) in storey 2 and (d) in storey 3.

are found to give rise to a 0.05% error in the luminosity [7].

In conclusion, no particular effect has been found which can explain the full −0.38% change in the luminosity when tightening the fiducial boundary, and no indication as to whether the tight boundary provides more correct results than the standard one. We have checked that it is not possible to define a stricter fiducial region which deviates more than 0.38% from the standard. As a conservative choice for the systematic error on the boundary simulation, 0.38% is taken, the largest observed difference due to a variation of the cut.

7.6 Non–fiducial Side Cut

Figure 12 shows the distribution of the shower position distance to the edge of the detector for the side with the loose geometrical cut, (a) for the standard definition of the fiducial region, and (b) with the fiducial region reduced by one padrow along the edge near the beam. Variations of the cut, normally at 10 mm, between 0 and 13 mm change the luminosity by a maximum of 0.15%. If the loose cut on the outer radius

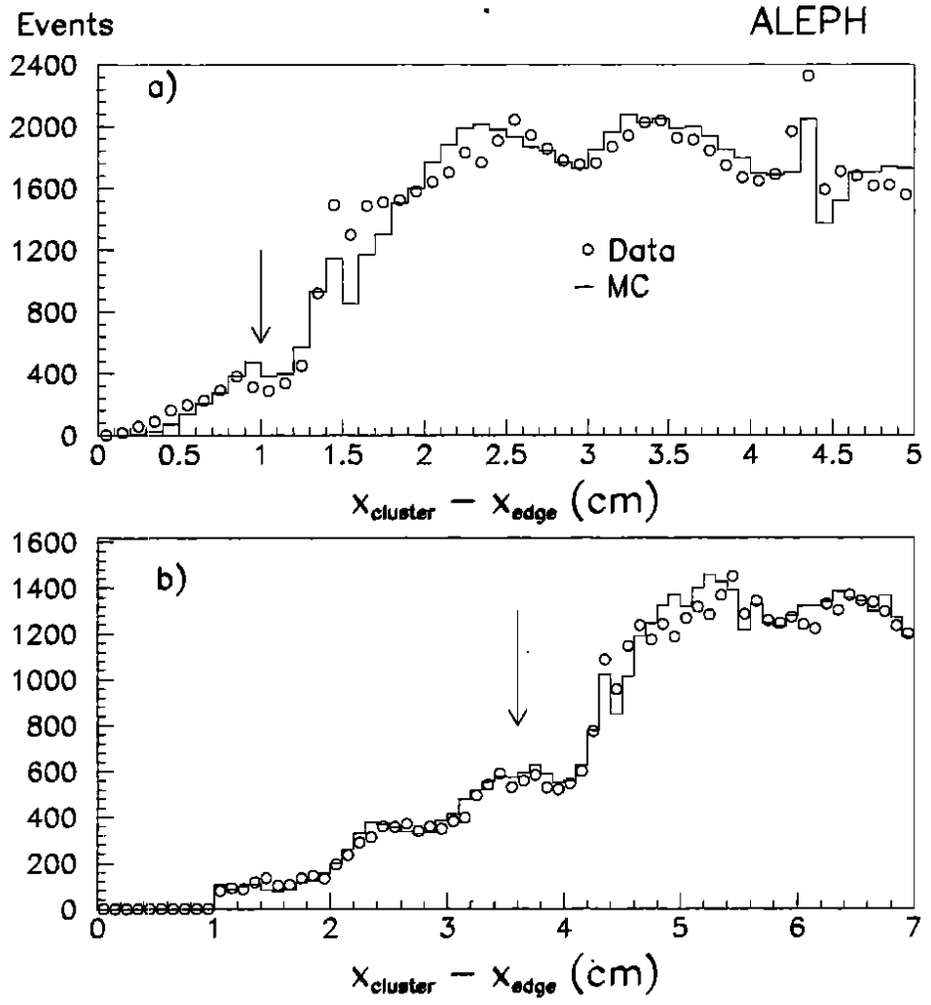

Figure 12: Distribution of the shower position distance to the edge of the detector on the non-fiducial side: (a) for the standard region boundaries, (b) for the tighter definition of the fiducial region wherein the fiducial boundary is moved one padrow away from the beamline. Arrows indicate the position of the cuts.

is removed no change in the luminosity is seen. The error introduced by this cut is therefore set to 0.15%.

7.7 Acoplanarity Cut

The acoplanarity $\Delta\phi$ could be affected by sudden pedestal shifts in the pad data which were present in isolated runs (about 5% the data). The effect was corrected by suppressing the energy from the affected storey and estimating its energy from the wire planes and unaffected storeys of the same tower. A simulation of the effect changed the luminosity in a test sample by $(0.10 \pm 0.05)\%$.

When the $\Delta\phi$ cut is relaxed to 150^0, the luminosity increases steadily with respect to nominal by 0.10%, which is taken to be the systematic error from the cut.

7.8 Energy Cut

As discussed in section 2.1.2, the distribution of cluster energies, for clusters fully contained in the calorimeter, is calibrated to peak at the beam energy. This fixes the beam energy point on the energy scale to better than 0.5%. A change of the energy cuts by $\pm 5\%$ would change the number of events by only $\pm 0.13\%$. Since the peak position in data and Monte Carlo agree within 0.1%, the error from the global energy scale is negligible.

Nonlinearity of the energy response can also contribute to the error, if it is not properly described in the Monte Carlo. Events near the cut either contain low energy particles, or they have suffered large energy losses. The cut is placed at an energy where the spectrum is flat. If the cut on the energy sum is varied between 0.50 to 0.78 of the total energy, and the cut on each leg is simultaneously varied between 0.36 to 0.56 of the beam energy, then the change in luminosity goes steadily from $(+0.14 \pm 0.02)\%$ to $(-0.22 \pm 0.04)\%$. An extrapolation of the change down to a cut at zero, assuming a constant ratio between data and Monte Carlo, yields +0.23%. Similar changes in luminosity expected from higher order corrections when moving the energy cuts are studied in section 9.

The internal wire supports of the calorimeter could present a risk of unsimulated energy losses. However, if their locations are left out of the luminosity calculation, then it changes by only $(0.07 \pm 0.12)\%$. Similarly, the support dowels of SATR degrade the energy somewhat. These are placed near cells forming the outer boundary of the fiducial region. Leaving out the entire outer boundary, i.e. reducing its radius by one cell, changes the luminosity by $(-0.03 \pm 0.06)\%$.

The combined error assigned from the energy cuts is 0.23%.

8 Luminosity Determination using the Tracking Chamber

In order to provide an independent check of the standard luminosity determination an alternative procedure was developed. The alternate procedure uses the LCAL only for the trigger and the energy measurement, and defines the geometrical acceptances with the SATR. Other than that, the philosophy of event selection remains the same. The acceptance regions, defined by SATR polar angle measurements, are from 60 to 80 mrad for the fiducial side and from 57.4 to 85 mrad for the non–fiducial side. The alternation of fiducial and non–fiducial sides on each trigger is applied as in the standard

selection. Additionally it is necessary to exclude an area corresponding to the vertical insensitive zone in LCAL ($\pm$ 3 cm on either side of the vertical axis). Finally, no cut on acoplanarity is needed since in this polar angle region background from off-momentum beam particles is negligible after energy cuts are applied.

8.1 Tracking Efficiency, Cross Section, and Background

In order to define the acceptance regions with SATR, a track in the tracking chamber must be associated with each of the two LCAL energy clusters. Thus track reconstruction efficiency is a critical quantity.

The efficiency for reconstructing events with two tracks is calculated using events with two back-to-back LCAL clusters well within the SATR acceptance. The track reconstruction efficiency is then determined as the ratio of the number of events with a track found on both sides to the total number of events. For real data and simulated data, efficiencies of $(96.23 \pm 0.06)\%$ and $(96.89 \pm 0.05)\%$ respectively, are obtained. The result is stable against changes in the acceptance region definition. The largest discrepancy, 0.2% in the ratio of the Monte Carlo efficiency to data efficiency, is observed when an acoplanarity cut of 10° on clusters is introduced. Thus, the ratio between the track reconstruction efficiencies for real data and Monte Carlo is $(99.33 \pm 0.08_{\mathrm{stat}} \pm 0.2_{\mathrm{syst}})\%$.

Background from all sources is almost nil in the angular range covered by SATR. The main contribution is from two photon processes and is approximately 0.015%, which is taken as the error due to background.

The reference cross section, with its experimental systematic error, after correcting for track reconstruction efficiency, is $(12.91 \pm 0.09_{exp})$ nb, roughly one half of the standard reference cross section.

8.2 Systematic uncertainties

The general agreement between data and Monte Carlo for the quantities determining the geometrical acceptance is illustrated in figure 13 where the polar angle and the absolute magnitude of the horizontal position of the track impact point are plotted.

As in the standard selection using LCAL, the systematic errors have been estimated by varying the cuts over a wide range in data and Monte Carlo and observing the change in luminosity. For the geometrical acceptance, the largest observed effect occurs when making the fiducial side angular region more restrictive. A difference of $(0.41 \pm 0.36)\%$ in luminosity is seen when the lower polar angle cut on the fiducial side is changed from 58 mrad to 65 mrad. This is taken as a conservative estimate of the uncertainty due to the geometrical acceptance definition.

The track position resolution is not perfectly simulated. By comparing track and cluster position the discrepancy between data and Monte Carlo resolution is found to introduce a 0.05% uncertainty on the luminosity.

The alignment procedure is identical to that used for LCAL. The uncertainty on the position of drift cell with respect to the centre of two modules is 0.1 mm which introduces a 0.3% uncertainty in the luminosity.

The uncertainty due to energy measurement is the same here as for the standard selection (see section 7.8), as is the uncertainty in the approximation of the energy

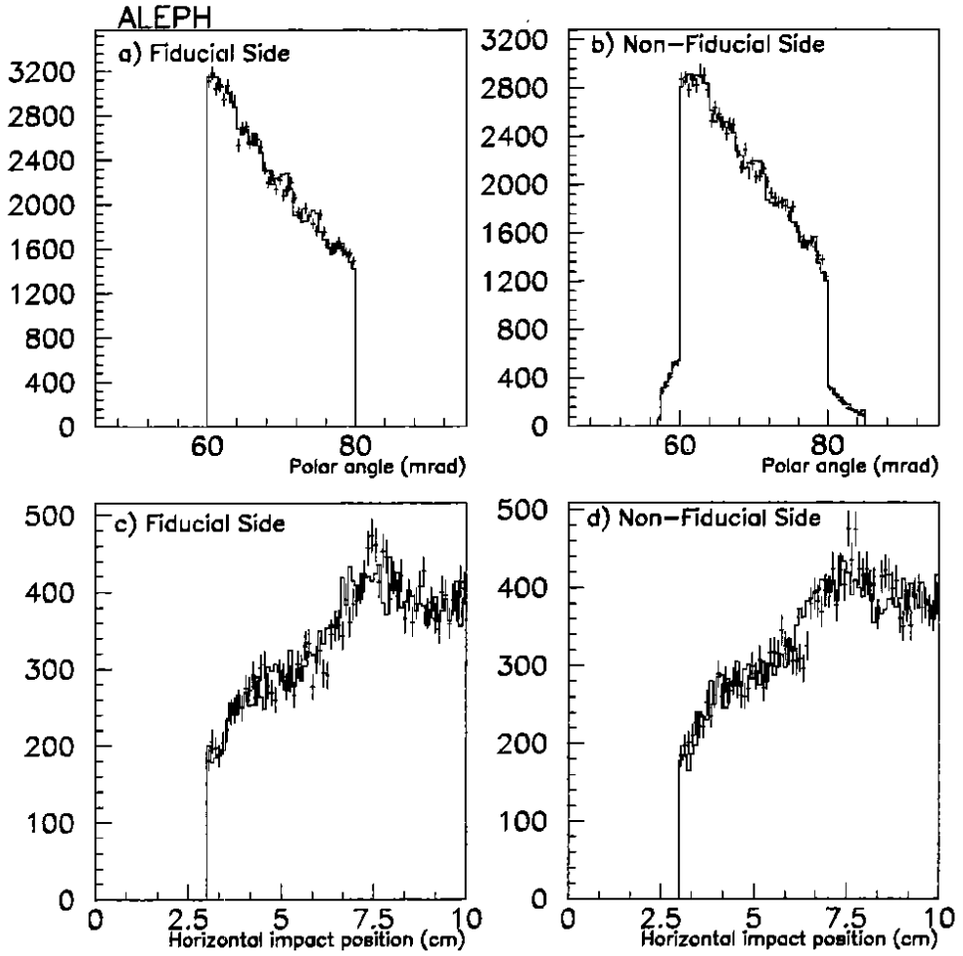

Figure 13: Comparison between data (plotted points) and Monte Carlo (solid histogram) for quantities determining the geometrical acceptance of the SATR. Distribution of polar angle on (a) the fiducial side and (b) the non–fiducial side. Absolute magnitude of track impact position projected onto the plane at $z = 280$ on (c) the fiducial side and (d) the non–fiducial side.

Background estimate	0.015 %
Internal alignment	0.30 %
External alignment and beam position	0.024 %
Track position resolution	0.05 %
Geometrical acceptance	0.41 %
LCAL energy scale, uniformity, resolution, trigger (sect. 7)	0.23 %
Track reconstruction efficiency	0.20 %
Approximation of energy dependence (sect. 6)	0.10 %
Statistics of simulation	0.27 %
Total experimental uncertainty for alternate method	0.7 %

Table 3: Summary of experimental systematic errors in the alternative luminosity determination using SATR to define the geometrical acceptance regions.

dependence of the cross section (see section 6).

The systematic errors of this alternative luminosity determination are summarized in table 3. By adding the contributions quadratically, one obtains 0.7% as the experimental uncertainty.

8.3 Comparison to Standard Method

Good agreement between the standard and the alternative method is seen. The relative systematic error of the difference between the two methods is 0.7%, estimated by removing common systematics including those from the energy measurement, external alignment and beam position. The ratio of the luminosities as determined by the alternative to the standard method, with its statistical error, is (1.001 ± 0.003), for all of the 1990 data. The ratio has no dependence on the centre of mass energy or time. This result may be interpreted as a test of the geometrical acceptance of the standard method.

9 Theoretical Predictions

The Monte Carlo event generator BABAMC [9] is used to calculate a basic theoretical prediction for the ALEPH luminosity cross section. The events from BABAMC are passed through the detector simulation and all comparisons of data and Monte Carlo are based on these events. Two corrections to this basic cross section are then calculated. The corrections affect only the magnitude of the cross section and not the events generated by BABAMC. The first correction amounts to an improvement of BABAMC to include a higher order treatment of photon vacuum polarization. The second correction is intended to account for higher order terms which are missing in BABAMC. Both corrections depend on the detector acceptance.

The BABAMC calculation is first order in α, and includes the dominant photon t-channel term, the interference term between the photon t-channel and the Z s-channel ($< 1\%$) and the small ($\approx .1\%$) interference term between the photon s- and t-channels.

One can classify the different contributions to theoretical calculations of QED according to different terms containing large logarithms. In the case of luminosity calculations

			Born 100% BABAMC,ALIBABA,LUMLOG
		(α/π) non-leading NL(α^1) 0.25% BABAMC, ALIBABA	$(\alpha/\pi)L$ leading-log LL(α^1) 8.19% BABAMC,ALIBABA,LUMLOG
	$(\alpha/\pi)^2$ 0.0006%	$(\alpha/\pi)^2 L$ next-to-leading-log NLL(α^2) 0.02%	$(\alpha/\pi)^2 L^2$ leading-log LL(α^2) 0.67% ALIBABA, LUMLOG
$(\alpha/\pi)^3$	$(\alpha/\pi)^3 L$ 0.0001%	$(\alpha/\pi)^3 L^2$ 0.002%	$(\alpha/\pi)^3 L^3$ leading-log LL(α^3) 0.055% LUMLOG

Table 4: Classification of QED contributions according to different terms containing large logarithms and their estimated values according to the formulae in the table using L=33. Those terms used in the text are explicitly named. The terms contained in the various programs are indicated.

this large logarithm L=2 $\times$ ln(t/m_e^2) $\sim$ 33, where t is a typical momentum transfer squared and the factor of 2 is also typical of the calculations. For different orders in α the dominant term is called leading-log (LL) and it contains the same number of powers of L as α/π. Other terms, with more powers of α/π than L are called next-to-leading-log (NLL) or non-leading (NL). The size of terms decreases exponentially with increasing powers of α/π and decreasing powers of L (see table 4).

9.1 Precision of BABAMC

In order to determine the precision of the first order calculation in BABAMC we have compared its results to a calculation of S. Jadach et al. [10] wherein special care has been taken to obtain a "technical precision" [3] of 0.02%. In this comparison vacuum polarisation and Z contributions in BABAMC were not used since they are absent in [10]. The values of first order corrections from the two programs agree to better than 0.1% when the k_0 parameter is set equal to 0.001. The results are different by about 0.2% for k_0 equal to 0.01. The small shift of about 0.1% both in the Born term and first order correction is due to interference between photon s- and t-channel terms which is present in BABAMC and absent in the calculation of [10].

Thus, the technical precision of BABAMC with the k_0 equal to 0.001 is better than 0.1%.

[3]Technical precision includes all the errors related to biases due to definition of hard and soft scattering regimes (the k_0 cut-off), integration approximations, quasi-randomness of random numbers, etc. It can be estimated by comparing two or more programs which are as independent as possible [10,11]. It does not include physics effects such as higher order corrections etc.

9.2 Higher Order Vacuum Polarization Corrections

In BABAMC the vacuum polarization is simply added as twice the real part of the photon vacuum polarization and only in the soft-radiation part of the calculation. This correction amounts to $\sim$+5.3% of the cross section in ALEPH. The well known procedure of Dyson summation [12] can account for higher order corrections and the corresponding formula should be applied as a multiplicative factor both in the soft and hard (bremsstrahlung) parts. To average the vacuum polarization and first order correction simultaneously over the t range covered, the photon treatment in BABAMC has been modified[4]. It is important to note that large cancellations exist between the hard and soft parts of the cross section; the k_0 dependence of BABAMC is not changed by our modification to the program. Using the modified BABAMC, the total correction from higher order vacuum polarization is (-0.23 ± 0.04)% within the ALEPH cuts.

A simple calculation yields a total correction of -0.14% where $\sim$+0.23% is in the soft part and ~ -0.37% in the hard part. For this simple calculation the Dyson sum of the vacuum polarization and the first order correction were averaged separately over the experimental acceptance in the hard contribution. This multiplication of mean values is a simplification but is in reasonable agreement with our full calculation.

9.3 Higher Order Bremsstrahlung Correction

We have used the generator LUMLOG written by S. Jadach et al. [11] to calculate a higher order bremsstrahlung correction to BABAMC. LUMLOG is a leading-log (LL) generator up to $O(\alpha^3)$ with bremsstrahlung (in the initial state only) and a technical precision of 2×10^{-4}. LUMLOG contains no non-leading terms at any order in α. In the calculation of the correction, the experimental energy cuts and the complicated geometrical acceptance of ALEPH were applied. A correction of (0.16 ± 0.02)% is found; the error is statistical.

A comparison between LUMLOG and the luminosity version of the ALIBABA [14] program was made [5]. ALIBABA contains LL terms to $O(\alpha^2)$ and the non-leading term at $O(\alpha^1)$. The overall precision of ALIBABA, combining physics limitations and technical precision, is 5×10^{-3}. In order to make this comparison the first order non-leading part, the vacuum polarization contributions, as well as the final state radiation in ALIBABA were not used. Further it was necessary to use geometrical cuts similar to those used in ALEPH, but much simpler, since ALIBABA is not an event generator but a semi–analytic calculation. A thorough comparison shows agreement between LUMLOG and ALIBABA at better than 0.1% for the higher order corrections.

Final state bremsstrahlung is set to zero in LUMLOG. This approach is justified by the Kinoshita–Lee–Nauenberg (KLN) theorem [16] which states, for our application, that since events with collinear final state photons cannot be separated experimentally from events with no photons, the LL final state correction vanishes. The non-leading $O(\alpha^1)$ correction is included in BABAMC. The next-to-leading $O(\alpha^2)$ correction is included in the error estimate in table 6. More discussion can be found in Ref. [11].

[4] We are grateful to R. Kleiss [13] for helping us to correct the hard bremsstrahlung part of the cross section.

[5] The ALIBABA results were kindly obtained for us by W. Beenakker [15].

	Standard Selection	Stricter Fiducial Cut	Lower Energy Cuts	Higher Energy Cuts
higher order vac. pol. cor. (%) (from modified BABAMC)	-0.23 ± 0.04	-0.23	-0.19	-0.31
($LL(\alpha^3)$ - $LL(\alpha^1)$) cor. (%) (from LUMLOG)	$+0.16 \pm 0.02$	$+0.09$	$+0.20$	$+0.07$
total correction (%)	$\mathbf{-0.07 \pm 0.05}$	$\mathbf{-0.15}$	$\mathbf{+0.01}$	$\mathbf{-0.24}$
Change with respect to standard selection (%)		-0.08	$+0.08$	-0.17

Table 5: Dependence of higher order corrections on experimental cuts. The first column is for the standard selection and shows the corrections actually applied to the BABAMC cross section (errors for the entries in the other columns are the same as those in the first column). The second column shows the correction when the fiducial boundary is moved one padrow away from the beamline. The last two columns display the effects of changing the energy cuts.

9.4 Dependence of Higher Order Correction on Experimental Cuts

In order to investigate the dependence of the theoretical corrections on the experimental cuts, we have calculated both the higher order bremsstrahlung correction and the higher order vacuum polarization correction for several different geometrical acceptances, and for various combinations of the energy cuts. The higher order leading-log correction to acoplanarity is identically zero.

Results are summarized in the table 5. The first column represents corrections for the standard ALEPH cuts which are applied to the BABAMC cross section. The second column corresponds to the change in fiducial acceptance which was applied to the data and Monte Carlo in section 7.5. In section 7.5 a change in luminosity of $(-0.38\pm 0.19)\%$ was found. This may be compared with the theoretically expected change of $(-0.08\pm 0.03)\%$. If in addition the non–fiducial boundary is moved such that the distance between fiducial and non–fiducial boundaries (as measured at the point nearest the beamline) varies between 0.9 cm and 3.5 cm no difference greater than 0.03% in the result is observed. All these corrections have been calculated at the particle level, without detector simulation, after which both angles and energies of particles may change. The quantity most affected by the detector and reconstruction is the distance of the cluster to the non-fiducial side boundary, which may change by about 3 mm. Therefore the error due to higher order corrections to the geometrical acceptance is conservatively estimated to be 0.1%.

The sensitivity of the higher order corrections to the energy cuts has been studied by varying the cuts in the same way as was done for the data in section 7.8. That is, the energy sum cut was varied between 0.50 and 0.78 of the total energy while the cut on each leg was varied between 0.36 and 0.56 of the beam energy (see the last two columns of table 5). Recall from section 7.8 that the experimental luminosity changed by $(+0.14 \pm 0.02)\%$ for the lowered cuts and by $(-0.22\pm0.04)\%$ for the raised cuts. The changes expected theoretically from higher order corrections are $(+0.08 \pm 0.04)\%$

NLL(α^2) QED bremsstrahlung [11]	0.2%
l^+l^- pair production [11]	0.1%
Vacuum polarization [17]	0.08%
Technical precision of BABAMC (sect.9.1)	0.1%
Higher order corrections to BABAMC (table 5)	0.05%
Technical precision of LUMLOG [11]	0.02%
Dependence on expt. cuts (sect. 9.4)	0.1%
Total error of theoretical prediction	0.3%

Table 6: Contributions to the theoretical error

for the lowered cuts and $(-0.17\pm0.04)\%$ for the raised cuts. The uncertainty in the theoretically predicted cross section due to the fact that energy cuts must be made on the data is a small fraction of the change we observe when varying the cuts in this way. Thus the theoretical uncertainty due to energy cuts is negligible with respect to the error of 0.1% from geometrical acceptance.

The results in table 5 suggest that some of the changes in luminosity observed when varying the experimental cuts may be explained by higher order corrections. We ignore these possible explanations.

9.5 Error on Theoretical cross section

In table 6 we summarize the various contributions to the theoretical error on the ALEPH luminosity cross section. The following comments should be made: the first two contributions describe the error due to physics not included in the present calculations and come from the paper of Jadach et al. [11]. The NLL(α^2) term is the largest term not included in the calculations (see table 4). The error from the hadronic vacuum polarization component was calculated based on the paper by Burkhardt et al. [17]. Finally, since the errors are independent they are added quadratically.

10 Conclusion

The luminosity in e^+e^- collisions has been measured for the 1990 running period of LEP by the ALEPH collaboration using a lead/gas proportional wire chamber calorimeter. Systematic checks have been made using a drift tube tracking chamber. The total systematic error on the measurement is 0.7%, with 0.6% coming from experimental uncertainties and 0.3% from theoretical uncertainties.

11 Acknowledegements

Progress in theoretical calculations of the low angle Bhabha cross section in ALEPH was possible thanks to many discussions with S. Jadach, E. Richter-Wąs, B.F.L. Ward and Z. Wąs. Comparisons with ALIBABA calculations have been made in collaboration with W. Beenakker. R. Kleiss has helped us with implementation of higher order vacuum polarization in BABAMC.

We are pleased to thank the SL division for their continuing success in operating LEP. Those of us from non-member states wish to thank CERN for its hospitality.

References

[1] A. Borrelli, M. Consoli, L. Maiani, and R. Sisto; Nucl. Phys. B333 (1990) 357.
M. Martinez, Ll. Garrido, R. Miquel, J.L. Harton, and R. Tanaka; Z. Phys. C490 (1001)645.
D. Bardin et al.; Nucl. Phys. B351 (1991) 1.

[2] "Improved Measurements of Electroweak Parameters from Z Decays into Fermion Pairs", D.Decamp et al. (The ALEPH Collaboration); CERN–PPE/91-105
To be published in Z. Phys. C.

[3] See for example F.A.Berends in "Z Physics at LEP I", G. Altarelli et al. (eds), CERN 89-08, 1989.

[4] G.S. Abrams et al. (The MARK II Collaboration), Phys. Rev. Lett. 63 (1989) 724
G.S. Abrams et al. (The MARK II Collaboration), Phys. Rev. Lett. 63 (1989) 2173
B Adeva et al. (The L3 Collaboration), Phys. Lett B231(1989) 509
D.Decamp et al. (The ALEPH Collaboration), Phys. Lett. B231(1989) 519
M. Z. Akrawy et al. (The OPAL Collaboration), Phys. Lett. B231(1989) 530
P Aarnio et al. (The DELPHI Collaboration), Phys. Lett. B231(1989) 539
D.Decamp et al. (The ALEPH Collaboration), Z. Phys C48 (1990) 365-391.
P. Aarnio et al. (The DELPHI Collaboration), Phys. Lett. B214(1990), P. Abreu et al. (The DELPHI Collaboration), Phys. Lett. B241 (1990) 435
B. Adeva et al. (The L3 Collaboration), L3 Preprint - 28 (1991)
G. Alexander et al. (The OPAL Collaboration), CERN–PPE/91–67

[5] D.Decamp et al. (The ALEPH Collaboration)
Nucl. Instrum. and Meths. A294 (1990) 121-178.

[6] H.Meinhard, Thesis, Universität - Gesamthochschule - Siegen, Germany, January 1991.

[7] L.Mirabito, Thesis, Université d'Aix-Marseille, France, February 1991.

[8] J.Wear, Thesis, University of Wisconsin-Madison, U.S.A., April 1991.

[9] M.Böhm, A.Denner, and W.Hollik; Nucl. Phys. B304 (1988) 687,
F.A Berends, R.Kleiss, and W.Hollik; Nucl. Phys. B304 (1988) 712,
Computer program BABAMC, courtesy of R.Kleiss.

[10] S.Jadach, E.Richter-Was, Z.Was, and B.F.L.Ward; Phys. Lett. B253 (1991) 469.

[11] S.Jadach, E.Richter-Was, Z.Was, and B.F.L.Ward; Phys. Lett. B260 (1991) 438.

[12] F. Halzen and A. D. Martin, "Quarks and Leptons", 1984, ed. by John Wiley and Sons, Inc., New York, section 7.8 .

[13] R. Kleiss, private communication.

[14] W.Beenakker, F.A.Berends, and S.C. van der Marck; Nucl. Phys B355 (1991) 281.

[15] W.Beenakker, private communication.

[16] T. D. Lee and M. Nauenberg; Phys. Rev. 133 (1964) 1549; T. Kinoshita; J. Math. Phys. 3 (1962) 650.

[17] H.Burkhardt, F. Jegerlehner, G. Penso, and C. Verzegnassi; Zeitschrift für Physik C43 (1989) 497.